

The Wardle Instability in Interstellar Shocks:

II. Gas Temperature and Line Emission

David A. Neufeld

Department of Physics & Astronomy, The Johns Hopkins University, Baltimore, MD 21218

and

James M. Stone

Department of Astronomy, University of Maryland, College Park, MD 20742

ABSTRACT

We have modeled the gas temperature structure in unstable C-type shocks and obtained predictions for the resultant CO and H₂ rotational line emissions, using numerical simulations of the Wardle instability that were carried out by Stone (1997) and that have been described in a companion paper. Our model for the thermal balance of the gas includes ion-neutral frictional heating; compressional heating; radiative cooling due to rotational and rovibrational transitions of the molecules CO, H₂O and H₂; and gas-grain collisional cooling. We obtained results for the gas temperature distribution in – and H₂ and CO line emission from – shocks of neutral Alfvénic Mach number 10 and velocity 20 or 40 km s^{–1} in which the Wardle instability has saturated. Both two- and three-dimensional simulations were carried out for shocks in which the preshock magnetic field is perpendicular to the shock propagation direction; and a 2-D simulation was carried out for the case in which the magnetic field is obliquely oriented with respect to the shock propagation direction. Although the Wardle instability profoundly affects the density structure behind C-type shocks, most of the shock-excited molecular line emission is generated upstream of the region where the strongest effects of the instability are felt. Thus the Wardle instability has a relatively small effect upon the overall gas temperature distribution in – and the emission line spectrum from – C-type shocks, at least for the cases that we have considered. In none of the cases that we have considered thus far did any of the predicted emission line luminosities change by more than a factor 2.5, and in most cases the effects of instability were significantly smaller than that. Slightly larger changes in the line luminosities seem likely for 3-D simulations of oblique shocks, although such simulations have yet to be carried out and lie beyond the scope of this study. Given the typical uncertainties that are always

present when model predictions are compared with real astronomical data, we conclude that Wardle instability does not imprint any clear observational signature on the shock-excited CO and H₂ line strengths. This result justifies the use of 1-D steady shock models in the interpretation of observations of shock-excited line emission in regions of star formation. Our 3-D simulations of perpendicular shocks revealed the presence of warm filamentary structures that are aligned along the magnetic field, a result of possible relevance to models of water maser emission from C-type shocks.

Subject headings: Infrared: ISM: Lines and Bands – ISM: Molecules – Molecular Processes – Shock Waves – Instabilities – Masers

1. Introduction

Shock waves have been recognized as a widespread phenomenon in regions of active star formation, where supersonic protostellar outflows interact with surrounding interstellar gas (Draine & McKee 1993, and references therein). Shock waves in star forming regions typically give rise to hot molecular gas at temperatures of several hundred to several thousand Kelvin that has been observed by means of the radiation it emits in high-lying rotational lines of CO (e.g. Watson et al. 1985; Genzel et al. 1988), in rovibrational transitions of H₂ (e.g. Brand et al. 1988), as well as pure rotational H₂ transitions (e.g. Wright et al. 1996).

Thus far, the most successful models (e.g. Draine & Roberge 1982; Chernoff, Hollenbach & McKee 1982; Draine, Roberge & Dalgarno 1983; Smith 1991; Kaufman & Neufeld 1996a, hereafter KN96) for these CO and H₂ emissions have invoked the presence of ‘Continuous-’ or C-type shocks (Draine 1980) in which the ionized and neutral species drift relative to each other but each show a *continuous* variation in flow velocity (in contrast to ‘Jump-’ or J-type shocks). Given the presence of magnetic fields of the strengths that are typically observed in the interstellar medium (Heiles et al. 1993), C-type shocks are expected to arise (Mullan 1971; Draine 1980) when shocks propagate at speeds less than $\sim 40 - 50 \text{ km s}^{-1}$ in molecular media of low fractional ionization. Models that invoke C-type shocks of speed $\sim 35 - 40 \text{ km s}^{-1}$ or (better) an admixture of shock speeds up to $\sim 40 \text{ km s}^{-1}$ (Smith & Brand 1990; Wright et al. 1996) have been successful in accounting quantitatively for the H₂ rovibrational line fluxes observed from the Orion-KL and Cepheus A (W) outflow regions and the CO line fluxes observed from Orion-KL. Models for C-type shocks in very dense molecular gas (Kaufman & Neufeld 1996b) have also been successfully invoked to explain

the radio and submillimeter wavelength water maser lines that have been observed in star forming regions.

To date, all models for the emission properties of C-type shocks have made use of one-dimensional time-independent solutions of the shock evolution equations, even though the semi-analytic work of Wardle (1990; 1991a,b) has established clearly that such solutions are subject to a rapidly-growing instability when the neutral Alfvénic Mach number exceeds ~ 5 (as it typically does in shock models for regions of active star formation). Numerical calculations by Toth (1994, 1995) of the non-linear evolution of the Wardle instability suggested that it leads to large amplitude compressions of the gas into structures that are elongated with the flow. In results described in a companion paper, Stone (1997, hereafter S97) has recently carried out two- and three-dimensional simulations that allow the nonlinear evolution of the Wardle instability to be followed to point where the instability saturates. These simulations allow us to address for the first time the question of how the Wardle instability affects the shock-excited line emission from C-type shocks. The question is important because if the effects were large then previous models for the line emission observed from such shocks would need to be revised.

In this paper, we present a study of the molecular line emission that is expected to result from unstable C-type shocks, given the ion and neutral velocity fields computed in the dynamical calculations of S97. In §2, we describe the details of our calculation, and in §3 we present and discuss the results obtained for three different geometries and two different shock velocities. The implications of our results are discussed in §4, and a brief summary is given in §5.

2. Calculations

In this study, we have computed the gas temperature and molecular line emission that is expected to result from unstable C-type shocks. Since thermal pressure does not significantly affect the dynamics in the magnetically dominated shocks that we have considered (c.f. S97), the dynamical and thermal calculations are effectively decoupled. The dynamical calculations upon which our study is based are summarized briefly in §2.1, and the computation of the gas temperature and the line emission are discussed in §2.2 and §2.3.

2.1. Dynamics

Our calculation of the gas temperature and line emission from unstable C-type shocks rests upon the dynamical calculations carried out recently by S97. Here the ionized and neutral species were treated as two interpenetrating but weakly-coupled fluids with separate velocity fields. The evolution of the gas is governed by five partial differential equations (Draine 1980; S97, equations 1–5) corresponding to mass conservation for the neutrals; mass conservation for the ions; momentum conservation for the ions (including the Lorentz force); momentum conservation for the neutrals; and flux-freezing of the magnetic field with respect to the ionized fluid. The neutral fluid is not subject to any Lorentz force but is coupled to the ionized fluid through a drag force $\alpha \rho_i \rho_n (\mathbf{v}_i - \mathbf{v}_n)$ per unit volume, where ρ_i and ρ_n are the mass densities of the ionized and neutral fluids; \mathbf{v}_i and \mathbf{v}_n are the bulk velocities of the ionized and neutral fluids; and α is a collisional coupling constant which, following Draine (1980), is assumed to be independent of the drift velocity $(\mathbf{v}_i - \mathbf{v}_n)$. The characteristic linear size of the shocked region is related to α by the expression

$$L_s \equiv \frac{v_{A,n}^0}{\alpha \rho_i^0}, \quad (1)$$

where $v_{A,n}^0$ is the preshock Alfvén speed in the neutral fluid, and ρ_i^0 is the preshock density of the ionized fluid.

The five partial differential equations that govern the evolution of the gas were solved numerically, using a new computer code, ZEUS-2F, that has been tested extensively in a variety of applications. A central feature of the numerical method is the implicit differencing of the (very stiff) ion-neutral drag terms so as to ensure their unconditional stability. Similar methods are being implemented independently by MacLow & Smith (1997). Two-dimensional simulations of C-type shocks were carried out for a variety of shock parameters typical of the dense interstellar medium, viz. Mach number $M = 40, 100$ or 200 ; neutral Alfvénic Mach number $A = 10$ or 20 ; angle between preshock magnetic field and flow direction $\theta = \pi/6, \pi/4$ or $\pi/2$. S97 also carried out a three-dimensional simulation for the single case $M = 100, A = 10, \theta = \pi/2$. In each case, the initial condition was the steady-state solution of the one-dimensional evolution equations.

While the shock parameters and results obtained in the dynamical calculation could be expressed in terms of dimensionless quantities, our calculation of the resultant gas temperatures and line emission requires the flow velocities and spatial coordinates to be expressed in dimensional units. In particular, the characteristic size scale $L_s = v_{A,n}^0 / (\alpha \rho_i^0)$ must be specified: given a preshock H_2 density of 10^5 cm^{-3} , the treatment of ion-neutral coupling presented by KN96 implies an effective value of $2.68 \times 10^{15} \text{ cm}$ for L_s . Our selection of the shock velocity and preshock magnetic field strength is discussed in §3 below.

2.2. Gas Temperature

Once the ion and neutral velocities in the shocked region have been computed, the gas temperature, T , may be determined by solving the energy equation for the neutral fluid:

$$\Lambda(T) = G - n_n k T \nabla \cdot \mathbf{v}_n - \nabla \cdot (u \mathbf{v}_n) - \partial u / \partial t, \quad (2)$$

where Λ is the gas cooling rate per unit volume, \mathbf{v}_n is the neutral velocity, $G = \alpha \rho_i \rho_n (\mathbf{v}_i - \mathbf{v}_n)^2$ is the frictional heating rate per unit volume, $n_n = \rho_n / \mu$ is the neutral particle density, μ is the mean particle mass, and u is the internal energy density of the gas. The four terms on the right represent frictional heating, compressional heating, the advection of thermal energy, and the effect of time-dependence in the internal energy. A considerable simplification is afforded by the fact that the cooling timescale within a C-type shock, $u / \Lambda(T)$, is necessarily short compared to the flow timescale. This allows the advection and time-dependent terms to be neglected, and the energy equation becomes an algebraic rather than a partial differential equation for T , the quantities G , n , and \mathbf{v}_n having already been determined in the numerical simulations of S97.

In computing the gas cooling function $\Lambda(T)$, we included cooling due to rotational and vibrational emissions from the molecules H_2 , H_2O and CO , adopting the radiative cooling functions of Neufeld & Kaufman (1993, hereafter NK93) and treating optical depth effects by an escape probability method described in the Appendix. Previous studies of gas-phase chemistry in C-type shocks (Draine et al. 1993; KN96), have indicated that for shock velocities greater than $\sim 15 \text{ km s}^{-1}$, atomic oxygen in the preshock gas is rapidly converted into water once the temperature reaches $\sim 400 \text{ K}$, while the preshock carbon monoxide abundance is unaffected by the passage of the shock. We have therefore assumed constant H_2O and CO abundances throughout the shocked region, adopting values relative to H_2 of 8.5×10^{-4} and 2.4×10^{-4} respectively (c.f. KN96). The cooling function $\Lambda(T)$ also includes the collisional energy transfer that results from inelastic collisions between gas molecules and grains, given an assumed grain temperature of 50 K ; for this process we adopted the gas-grain cooling rate of Hollenbach & McKee (1989).

2.3. Line emission

After determining the temperature structure of the shocked region, we computed the emission line spectrum. We solved the equations of statistical equilibrium for CO and H_2 for 36,000 different values of T , n_n , and an optical depth parameter \tilde{N} (c.f. Appendix), and then interpolated between the solutions thereby obtained to determine the H_2 level populations and CO line emissivities at every point in the shock simulation. Integrating

over the entire volume in which the gas temperature exceeds the dust temperature, we obtained predictions for the CO line luminosity from the warm shock-heated gas and for the column densities in various rotational states of H₂.

In solving the equations of statistical equilibrium for the CO level populations, we treated the effects of radiative trapping using the the same escape probability approximation that was used to compute the total radiative cooling rates (c.f. Appendix). We adopted the same molecular data for CO and H₂ that were used by KN96.

3. Results

In the present paper, we have confined our attention to the “fiducial” shock parameters considered by S97 (i.e. to shocks with Mach number $M = 100$ and neutral Alfvenic Mach number $A = 10$) and to the case where the preshock H₂ density is 10^5 cm^{-3} . All our results apply to shocks that are initially plane-parallel and that propagate in an initially homogeneous medium.

We obtained results for three different geometries: 2-D simulations of perpendicular shocks ($\theta = \pi/2$), 2-D simulations of oblique shocks ($\theta = \pi/6$), and 3-D simulations of perpendicular shocks. We also considered two different shock velocities: $v_s = 20$ and 40 km s^{-1} . Note however, that the assumed neutral Alfvenic Mach number was 10 for both shock velocities so the preshock magnetic fields we assumed were different in the two cases: the assumed field strengths were 0.45 and 0.89 mG respectively for the 20 and 40 km s^{-1} shocks.

For each of the six resultant cases, we have computed the gas temperatures in the shocked region and the predicted CO and H₂ line emissions for two snapshots: (1) the initial state in which the flow solution is the steady-state solution to the 1-D dynamical equations; and (2) after the Wardle instability has reached saturation. A crucial feature of the results presented here is that an identical method (with identical microphysical assumptions and approximations) was used for each snapshot; thus any differences in the predicted gas temperatures and line emissions for the second snapshot are directly attributable to the effects of the Wardle instability.

3.1. Gas temperatures

In Figure 1a (color plate), we present temperature and density maps for neutral species (i.e. molecular hydrogen) in two-dimensional simulations of a perpendicular shock

of velocity $v_s = 20 \text{ km s}^{-1}$. The upper panel shows the results for a steady shock (initial condition; elapsed time $t = 0$) and the lower panel shows the results after the Wardle instability has saturated ($t = 7 t_{flow} = 3000 \text{ yr}$). The left side of each panel shows the H_2 density and the right side shows the H_2 temperature. In each case, the preshock gas is located at the top of the panel and flows downwards relative to the shock.

In the initial state, the temperature structure agrees well with the earlier one-dimensional steady shock calculations of KN96. The agreement is not exact, however, because in the present study we have simplified slightly the detailed treatment of the microphysics undertaken by KN96 (c.f. §2.2). In particular, we have (1) neglected the advection term in the energy equation; (2) assumed a constant water abundance throughout the computational volume; and (3) neglected the dependence of the collisional coupling constant α upon the ion-neutral drift velocity. Despite these approximations, the differences between the temperature structure in the initial state and that predicted by KN96 are small: the peak temperatures in the shocked region are respectively 1160 and 1150 K, and the predicted fluxes for far-infrared CO lines ($J = 14 - 13$ and above) differ by at most 30% (c.f. §3.2 below).

As discussed by S97, the Wardle instability leads to the formation of dense sheets in which the neutral particle density is very much larger than the postshock density in a 1-D steady shock. These dense sheets are readily apparent on the left side of the lower panel. The right side of that panel, however, shows that those dense sheets are very cold; thus they are not expected to contribute to the high-temperature line emission that is characteristic of interstellar shocks. Outside the dense sheets, the effect of the instability upon the temperature structure is modest. Hot spots form where the incoming gas hits the edges of the dense sheets, and the peak temperature increases from 1160 K in the initial state to 1420 K after the Wardle instability has saturated, but the volume occupied by the hot spots is rather small. These results are discussed further in §4 below.

Analogous results are presented for a 2-D simulation of an oblique shock in Figure 1b (color plate), and for a 3-D simulation of a perpendicular shock in Figure 2 (color plate). As in the 2-D simulation of a perpendicular shock, the effects upon the high-temperature part of the shock are modest. In the 3-D simulations, however, additional instability modes are apparent. In particular, the Wardle instability results in filaments oriented along the magnetic field and perpendicular to the cold dense sheets in which the heating rate (c.f. S97) and the temperature are enhanced. The possible implications of this result for the generation of water maser emission in C-type shocks is discussed in §4.

We have found an alternative representation of the temperature structure to be a very useful supplement to Figures 1a, 1b, and Figure 2. In Figures 3a and 3b we have

characterized the temperature distribution in the shocked gas by plotting the column density of H_2 hotter than a given temperature, T , as a function of that temperature. The column density is an average along the shock propagation direction. The results shown in Figure 3a apply to perpendicular shocks of velocity 20 and 40 km s^{-1} , while those in Figure 3b apply to oblique shocks. Dotted lines show the temperature distributions for the initial state, corresponding to the steady-state solution for a one-dimensional shock. Solid lines show the results of 2-D simulations after the Wardle instability has saturated, and the dashed line (Figure 3a only) shows the result of a 3-D simulation.

Figures 3a and 3b show that although the Wardle instability increases the maximum temperature in the postshock gas, only a small H_2 column density ($\sim 10^{19} \text{ cm}^{-2}$) is present at temperatures higher than those achieved in an steady-state 1-D shock. In fact, the temperature of the warmest $\sim 10^{20} \text{ cm}^{-2}$ of H_2 is typically somewhat *smaller* in simulations where the Wardle instability has saturated. On the other hand, the Wardle instability tends to increase slightly the temperature in the region far downstream from the temperature peak so that the column density of gas warmer than 300 K is increased by up to a factor 2.

3.2. Line emission

Figures 4a and 4b show the expected CO emission for perpendicular and oblique shocks. Here the fluxes (i.e. luminosities per unit surface area of the shock) for pure rotational lines of CO are plotted as a function of the rotational quantum number of the upper state of the transition, J_U . As before, the dotted lines show results for the initial snapshot, corresponding to the steady-state solution for a one-dimensional shock. Solid lines show the results of 2-D simulations after the Wardle instability has saturated, and the dashed line (Figure 4a only) shows the result of a 3-D simulation. Analogous results for H_2 rotational states are shown in Figures 5a and 5b, in which the column densities of H_2 in different states of rotational excitation, N_J , have been divided by the statistical weight, g_J , and plotted as a function of the energy of the rotational state, E_J (in temperature units E_J/k). The meaning of the different line types is identical to that adopted in Figures 3a, 3b, 4a, and 4b. Since the quadrupole-allowed rotational transitions of H_2 are all optically-thin, the results shown in Figures 5a and 5b specify the predicted H_2 rotational line strengths unambiguously.

In addition to the C-type shocks from which we have computed the line emission, S97 found that the Wardle instability may also give rise to J-type shocks (in a region that has been advected out of the computational volume used here). Although interesting in their own right, these J-type shocks are expected to make a negligible contribution to the total

line emission, because the shock velocity is small ($\sim 1 \text{ km s}^{-1}$) and the energy dissipated within the J-type shocks amounts less than 1% of that dissipated in the C-type shocks modeled here.

Figures 4a, 4b, 5a, and 5b show that the effects of the Wardle instability upon the shock-excited emission lines fluxes are quite modest, and follow the behavior that would be expected from the temperature distributions plotted in Figures 3a and 3b. At least for the cases that we have considered thus far, the H_2 and high-J CO line strengths are changed by at most a factor 2.5, and in most cases the effect of the Wardle instability is considerably smaller than that. Since the effects of the Wardle instability upon the line luminosities were found to be (1) somewhat larger in oblique shocks than in perpendicular shocks and (2) slightly larger in 3-D simulations of perpendicular shocks than in 2-D simulations, we speculate that effects slightly larger than a factor 2.5 are likely for 3-D simulations of oblique shocks. Future numerical simulations of 3-D oblique shocks will be needed to test this speculation; unfortunately, such computations will involve a numerical expense significantly larger than that for any of the calculations carried out thus far by S97.

4. Discussion

The primary result of this study is a negative one. At least for the range of parameters and geometries that we have considered here, we conclude that *the Wardle instability does not imprint any clear observational signature upon the shock-excited CO and H_2 line spectra*, given the comparable or larger effects that may result from (1) uncertainties in the microphysics of ion-neutral coupling and molecular excitation; (2) observational errors in the measurement of line fluxes; (3) the superposition of shocks of different velocities in the telescope beam; (4) inhomogeneities in the preshock density; and so forth. This result provides a justification for the use of one-dimensional steady shock models in the interpretation of observations of shock-excited line emission.

The rather surprising negative result that we have obtained requires some explanation, particularly in light of the profound effects upon the postshock density structure that result from the Wardle instability. Figure 6 provides a graphical explanation of why the effects of the Wardle instability upon the shocked-excited line emission are relatively small. Here we plot the ion-neutral drift speed, $v_d = |\mathbf{v}_i - \mathbf{v}_n|$, and the compression of the ionized fluid, $C_i = \rho_i/\rho_i^0$, as a function of displacement along the shock propagation direction. The heating rate per neutral particle is proportional to $v_d^2 C_i$. Results are shown for a 1-D steady-state shock (dotted line), and for a trajectory that intersects the tip of a dense sheet within a 2-D perpendicular shock in which the Wardle instability has

saturated. In each case, the displacement is expressed relative to the location at which the temperature peaks, negative values referring to the preshock side. As Figure 6 shows, the final compression of the ions is increased enormously by the Wardle instability; however, by the time that the neutral particles reach the region of enhanced ion density, the drift velocity has dropped significantly. Most of the shock-excited line emission arises upstream of the region where the effects of the Wardle instability are felt. Indeed, the maximum heating rate per neutral particle is enhanced by only a relatively small factor even along trajectories that hit the dense sheets edge-on.

Despite the lack of an obvious signature in the spectrum of shock-excited line emission, our 3-D simulation of the Wardle instability in a perpendicular shock does predict an distinctive phenomenon: the formation of hot filaments that are oriented *along* the magnetic field and perpendicular to the cold dense sheets. At least in the perpendicular shock case that we have considered so far, these filaments are aligned perpendicular to the direction of maximum velocity gradient, yielding a long coherent path length for the amplification of maser radiation. This result is potentially important, because C-type shocks in very dense molecular gas have been proposed (Neufeld & Melnick 1990; KN96) as a likely source of the water maser emission observed in regions of active star formation. Further study is needed to determine (1) what maser emission properties would be expected from these filaments; and (2) whether the filaments are apparent in 3-D simulations of *oblique* shocks.

5. Summary

1. We have modeled the neutral gas temperature and the CO and H₂ rotational line emissivities in unstable C-type shocks, using numerical simulations of the Wardle instability that were carried out by Stone (1997) and described in a companion paper. The results apply to shocks that are initially plane-parallel and that propagate in an initially homogeneous medium.

2. In modeling the gas temperature within the shocked gas region, we included ion-neutral frictional heating, compressional heating, radiative cooling due to rotational and rovibrational transitions of the molecules CO, H₂O and H₂, and gas-grain collisional cooling. In modeling the line emission from CO and H₂ we solved the equations of statistical equilibrium for the populations in excited rotational states, using an escape probability method to treat the effects of radiative trapping in the CO transitions.

3. We obtained results for the gas temperature distribution in – and H₂ and CO line emission from – shocks of neutral Alfvénic Mach number 10 and velocity 20 or 40 km s^{–1}

in which the Wardle instability has saturated. Both two- and three-dimensional simulations were carried out for shocks in which the preshock magnetic field is perpendicular to the shock propagation direction; and a two-dimensional simulation was carried out for the case in which the magnetic field is obliquely oriented with respect to the shock propagation direction.

4. Although the Wardle instability profoundly affects the density structure behind C-type shocks, most of the shock-excited molecular line emission is generated upstream of the region where the strongest effects of the instability are felt. Thus the Wardle instability has a relatively small effect upon the overall gas temperature distribution in – and the emission line spectrum from – C-type shocks, at least for the cases that we have considered. In none of the cases that we have considered thus far did any of the predicted emission line luminosities change by more than a factor 2.5, and in most cases the effects of instability were significantly smaller than that. Slightly larger changes in the line luminosities seem likely for 3-D simulations of oblique shocks (c.f. §3.2 above), although such simulations have yet to be carried out and lie beyond the scope of this paper. Given the comparable or larger uncertainties in the microphysics, observational errors in the measurement of line fluxes, and uncertainties in the physical parameters for real interstellar regions where shocks are present, we conclude that Wardle instability does not imprint any clear observational signature on the shock-excited CO and H₂ line strengths. This result provides a justification for the use of one-dimensional steady shock models in the interpretation of observations of shock-excited line emission.

5. Our three-dimensional simulations of perpendicular shocks revealed the presence of warm filamentary structures that are aligned along the magnetic field, a result of possible relevance to models of water maser emission from C-type shocks.

6. The results presented in this paper apply to only a rather limited region of parameter space, and the conclusions of this study may not be generally applicable throughout the parameter space of astrophysical interest. In particular, future work will be needed to investigate the effects of the Wardle instability in 3-D simulations of oblique shocks, in bow shocks, and in shocks that propagate in inhomogeneous or weakly-magnetized media.

Acknowledgments

D. A. N. gratefully acknowledges the hospitality of the University of Maryland, College Park, where he was a sabbatical visitor during the period when this study was conceived and started. He also acknowledges with gratitude the support of NASA grant NAGW-3147

from the Long Term Space Astrophysics Research Program and of a National Science Foundation Young Investigator award. J. M. S. gratefully acknowledges the support of NSF grant AST-9528299.

Appendix: Treatment of optical depth effects

The volume cooling rate Λ (§2.2) depends not only upon the temperature but also upon the gas density and the optical depth in CO and H₂O line transitions that contribute to the cooling. NK93 used an escape probability method to treat optical depth effects, making use of the Sobolev approximation to model the escape of radiation from a one-dimensional fluid flow in which the velocity gradient is large. They introduced an optical depth parameter $\tilde{N} \equiv n_n/|dv_x/dx|$ to characterize the importance of optical depth effects. In the two- and three-dimensional velocity fields considered in the present paper, this expression for \tilde{N} must be generalized by the replacement of $|dv_x/dx|$ by an appropriate expression involving the velocity gradient tensor, $\partial v_{ni}/\partial x_j$.

In general, the optical depth parameter is inversely proportional to $\langle |dv_{ns}/ds| \rangle$, where $|dv_{ns}/ds|$ is the line-of-sight neutral velocity gradient along a given ray and $\langle \rangle$ denotes an angle-average. For a 1-D flow, $\langle |dv_{ns}/ds| \rangle = |dv_{nx}/dx|/3$. For a 3-D flow, we may write $\langle |dv_{ns}/ds| \rangle = (|e_1| + |e_2| + |e_3|)f/3$, where e_1 , e_2 and e_3 are the eigenvalues of the symmetrized velocity gradient tensor, $(\partial v_{ni}/\partial x_j + \partial v_{nj}/\partial x_i)/2$, in descending order of magnitude, and f is a number of order unity that depends upon e_2/e_1 and e_3/e_1 . Thus the expression for the optical depth parameter becomes $\tilde{N} \equiv n_n/f(|e_1| + |e_2| + |e_3|)$. By direct integration of dv_{ns}/ds over all angles, we have evaluated f in the limit where $e_3/e_1 \ll 1$ (a limit which applies exactly in 2-D flows and to good approximation in the 3-D flows of present interest). We find that f always lies in the range $2/\pi$ to 1, and is given by

$$f = 1 \quad (e_2/e_1 \geq 0)$$

$$f = \frac{1-R}{1+R} + \frac{4}{\pi} \left(\frac{R}{1+R^2} - \frac{1-R}{1+R} \tan^{-1} R \right) \quad (e_2/e_1 \leq 0),$$

where $R = -e_2/e_1$.

References

- Brand, P.W.J.L., Moorehouse, A., Bird, M., Burton, M.G., & Geballe, T.R. 1988, *ApJ*, 334, L103.
- Chernoff, D.F., Hollenbach, D.J., & McKee, C.F. 1982, *ApJ*, 259, L97.
- Draine, B.T. 1980, *ApJ*, 241, 1021.
- Draine, B.T., & McKee, C.F. 1993, *ARA&A*, 31, 373.
- Draine, B.T., & Roberge, W.G. 1982, *ApJ*, 259, L91.
- Draine, B.T., & Roberge, W.G., & Dalgarno, A. 1983, *ApJ*, 264, 485.
- Genzel, R., Poglitsch, A., & Stacey, G.J. 1988, *ApJ*, 333, L59.
- Heiles, C., Goodman, A.A., McKee, C.F., & Zweibel, E.G. 1993, in *Protostars and Planets III*, ed. M. Matthews & E. Levy (Tucson: Univ. of Arizona Press).
- Hollenbach, D.J., & McKee, C.F. 1989, *ApJ*, 342, 306.
- Kaufman, M.J., & Neufeld, D.A. 1996a, *ApJ*, 456, 611 (KN96).
- Kaufman, M.J., & Neufeld, D.A. 1996b, *ApJ*, 456, 250.
- MacLow, M.-M., & Smith, M.D. 1997, *ApJ*, submitted.
- Mullan, D.J. 1971, *MNRAS*, 153, 145.
- Neufeld, D.A., & Kaufman, M.J. 1993, 418, 263 (NK93).
- Neufeld, D.A., & Melnick, G.J. 1990, *ApJ*, 352, L9.
- Smith, M.D. 1991, *MNRAS*, 253, 175.
- Smith, M.D., & Brand, P.W.J.L. 1990, *MNRAS*, 242, 495.
- Stone, J.M. 1997, *ApJ*, submitted (S97).
- Tóth, G. 1994, *ApJ*, 425, 171.
- Tóth, G. 1995, *MNRAS*, 274, 1002.
- Wardle, M. 1990, *MNRAS*, 246, 98.
- Wardle, M. 1991a, *MNRAS*, 250, 523.
- Wardle, M. 1991b, *MNRAS*, 251, 119.

Watson, D.M., Genzel, R., Townes, C.H., & Storey, J.W.V. 1985, ApJ, 298, 316.

Wright, C.M., Drapatz, S., Timmermann, R., van der Werf, P.P., Katterloher, R., & de Graauw, Th. 1996, A& A, 315, L301

Figure captions

Fig. 1a – Temperature and density maps for molecular hydrogen in two-dimensional simulations of a perpendicular shock ($\theta = \pi/2$) of velocity $v_s = 20 \text{ km s}^{-1}$, Alfven Mach number $A = 10$, and preshock H_2 density 10^5 cm^{-3} . The upper panel shows the results for a steady shock (initial condition; elapsed time $t = 0$) and the lower panel shows the results after the Wardle instability has saturated ($t = 7 t_{flow} = 3000 \text{ yr}$). The left side of each panel shows the H_2 density and the right side shows the H_2 temperature. In each case, the preshock gas is located at the top of the panel and flows downwards relative to the shock.

Fig. 1b – Same as for 1a but for an oblique shock ($t = 3.4 t_{flow} = 1640 \text{ yr}$ in lower panel).

Fig. 2 – Temperature map for molecular hydrogen in three-dimensional simulations of a perpendicular shock ($\theta = \pi/2$) of velocity $v_s = 20 \text{ km s}^{-1}$, Alfven Mach number $A = 10$, and preshock H_2 density 10^5 cm^{-3} . The figure shows the temperature structure after the Wardle instability has saturated ($t = 9.6 t_{flow} = 4100 \text{ yr}$).

Fig. 3a – Temperature distribution in the neutral fluid. The column density of shock-heated H_2 warmer than gas temperature T is plotted as a function of T for a perpendicular shocks ($\theta = \pi/2$) with Alfven Mach number $A = 10$, preshock H_2 density 10^5 cm^{-3} , and shock velocity $v_s = 20$ and 40 km s^{-1} . Dotted lines show the results for a steady shock (initial condition; elapsed time $t = 0$), and solid lines show the results of two-dimensional simulations in which the Wardle instability has saturated ($t = 7 t_{flow} = 3000 \text{ yr}$). Dashed lines apply to three-dimensional simulations in which the Wardle instability has saturated ($t = 9.6 t_{flow} = 4100 \text{ yr}$).

Fig. 3b – Same as for 3a but for an oblique shock (2-D simulations only).

Fig. 4a – CO rotational emission from the shock-heated gas. The CO line fluxes are plotted as a function of the quantum number of the upper state, J_U . Results apply to perpendicular shocks ($\theta = \pi/2$) with Alfven Mach number $A = 10$, preshock H_2 density 10^5 cm^{-3} , and shock velocity $v_s = 20$ and 40 km s^{-1} . Dotted lines show the results for a steady shock (initial condition; elapsed time $t = 0$), and solid lines show the results of two-dimensional simulations in which the Wardle instability has saturated ($t = 7 t_{flow} = 3000 \text{ yr}$). Dashed lines apply to three-dimensional simulations in which the Wardle instability has saturated ($t = 9.6 t_{flow} = 4100 \text{ yr}$).

Fig. 4b – Same as for 4a but for an oblique shock (2-D simulations only).

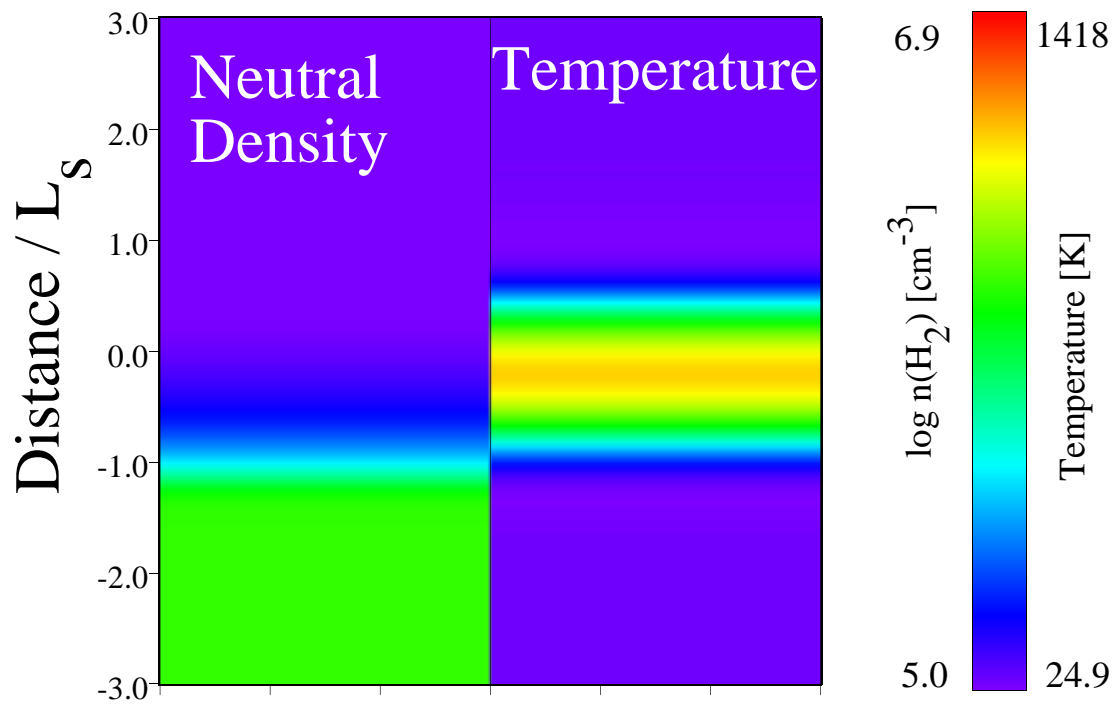
Fig. 5a – Rotational level populations of molecular hydrogen in the shock-heated gas. Column densities of H_2 in different states of rotational excitation, N_J , have been divided

by the statistical weight, g_J , and plotted as a function of the energy of the rotational state, E_J (in temperature units E_J/k). Results apply to perpendicular shocks ($\theta = \pi/2$) with Alfvén Mach number $A = 10$, preshock H_2 density 10^5 cm^{-3} , and shock velocity $v_s = 20$ and 40 km s^{-1} . Dotted lines show the results for a steady shock (initial condition; elapsed time $t = 0$), and solid lines show the results of two-dimensional simulations in which the Wardle instability has saturated ($t = 7 t_{flow} = 3000 \text{ yr}$). Dashed lines apply to three-dimensional simulations in which the Wardle instability has saturated ($t = 9.6 t_{flow} = 4100 \text{ yr}$).

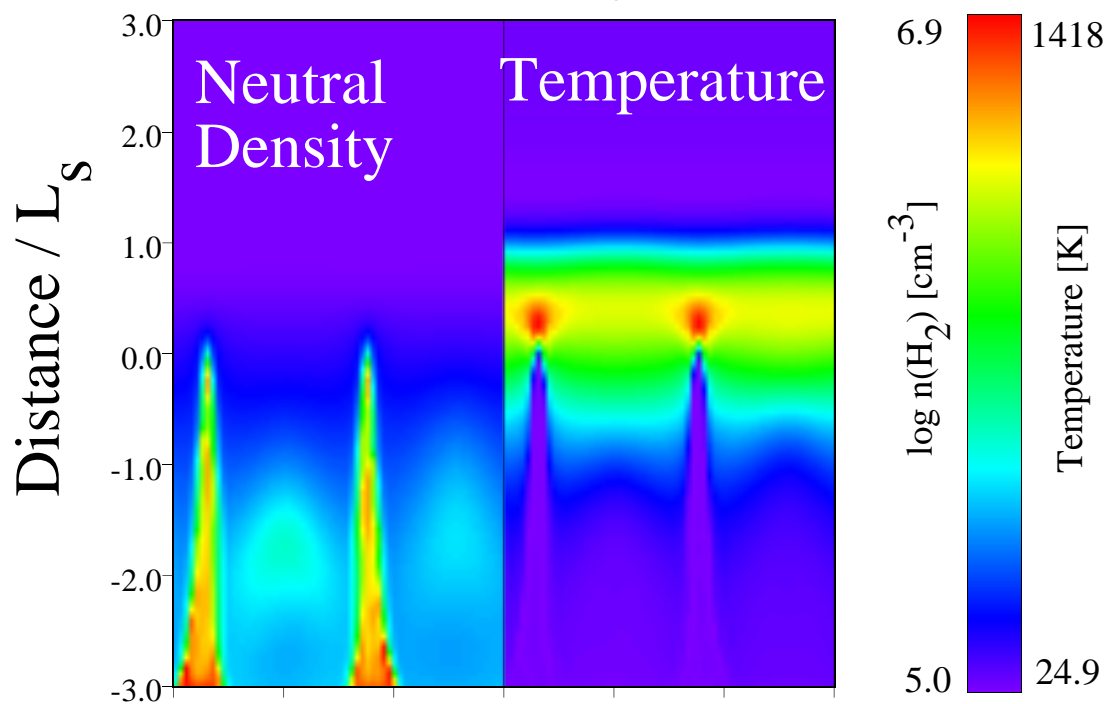
Fig. 5b – Same as for 5a but for an oblique shock (2-D simulations only).

Fig. 6 – Ion-neutral drift speed, $v_d = |\mathbf{v}_i - \mathbf{v}_n|$, and the compression of the ionized fluid, $C_i = \rho_i/\rho_i^0$, as a function of displacement along the shock propagation direction. The heating rate per neutral particle is proportional to $v_d^2 C_i$. Results are shown for a 1-D steady-state shock (dotted line), and for a trajectory that intersects the tip of a dense sheet within a 2-D perpendicular shock in which the Wardle instability has saturated. In each case, the displacement is expressed relative to the location at which the temperature peaks, negative values referring to the preshock side.

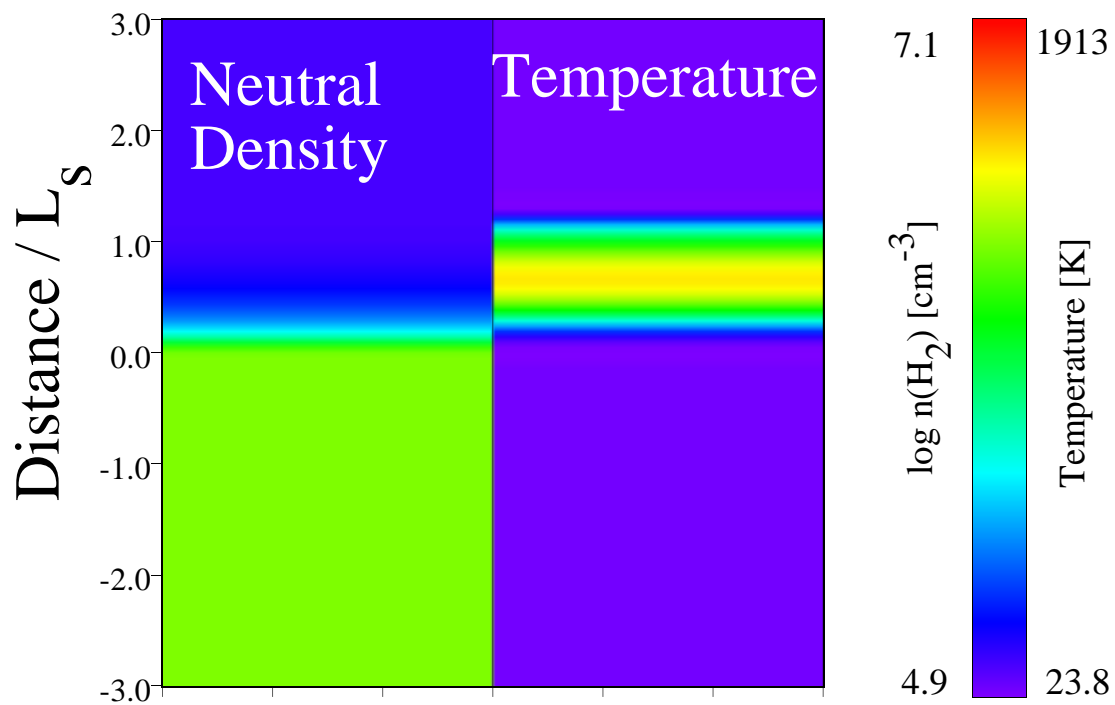
$t = 0$ (Steady Shock Solution)



$t = 3000$ yrs



$t = 0$ (Steady Shock Solution)



$t = 1640$ yrs

